C. R. Acad. Sci. Paris, t. 2, Série IV, p. 1193–1212, 2001
Physique appliquée/*Applied physics*
(Biophysique/*Biophysics*)

IMAGERIE ACOUSTIQUE ET OPTIQUE DES MILIEUX BIOLOGIQUES
OPTICAL AND ACOUSTICAL IMAGING OF BIOLOGICAL MEDIA

Elastography

Jonathan OPHIR [a,b], Faouzi KALLEL [a], Tomy VARGHESE [a,e], Elisa KONOFAGOU [a,f], S. Kaisar ALAM [a,g], Thomas KROUSKOP [c], Brian GARRA [d], Raffaella RIGHETTI [a,b]

[a] **University of Texas Medical School at Houston, Houston, TX, USA**
[b] **University of Houston, Department of ECE, Houston, TX, USA**
[c] **Baylor College of Medicine, Houston, TX, USA**
[d] **University of Vermont, Fletcher Allen Medical Center, Burlington, VT, USA**
[e] **University of Wisconsin, Madison, WI, USA**
[f] **Brigham and Women's Hospital, Boston, MA, USA**
[g] **Riverside Research Institute, New York, NY, USA**

(Reçu le 15 juin 2001, accepté le 28 juillet 2001)

Abstract. We present a concise summary of some of the fundamentals and of our work in the field of elastography over the past 12 years. This summary is not exhaustive, since several recent reviews of this area are available. We begin by presenting some relevant background material from the field of biomechanics, which forms the foundation of this work. We then proceed to discuss the basic principles and limitations that are involved in the production of strain images (elastograms) of biological tissues. Early results as well as current results from biological tissues in vitro and in vivo are shown. We conclude with some thoughts regarding the potential of elastography for medical diagnosis. © 2001 Académie des sciences/Éditions scientifiques et médicales Elsevier SAS

elastography / ultrasound / stress / strain / imaging / elasticity / shear modulus / Young's modulus

Élastographie

Résumé. *Nous présentons dans ce papier une revue du travail fait par notre équipe sur l'élastographie pendant ces* 12 *dernières années. Nous présentons d'abord des rappels de base sur la biomécanique. Nous discutons ensuite des principes de base et des limitations des techniques de l'imagerie du champ des déformations des milieux biologiques. Nous montrons ensuite les résultats obtenus in vitro et in vivo avec cette technique. Enfin nous concluons sur les perspectives des techniques d'élastographie en médecine. © 2001 Académie des sciences/Éditions scientifiques et médicales Elsevier SAS*

élastographie / ultrasons / contrainte / déformation / imagerie / élasticité / module de cisaillement / module d'Young

1. Introduction

In contrast to engineering materials, the mechanical properties of biological tissues are not easily definable by closed-form mathematical expressions. When living, tissues are metabolically active and

Note présentée par Guy LAVAL.

S1296-2147(01)01255-0/FLA

exhibit certain mechanical properties, which change soon after death. Moreover, these mechanical properties may be dependent on age, strain rate and strain range [1–3]. To simplify the characterization of a tissue when the loading is of short enough duration that the viscous nature of the material can be ignored, the tissue can be assumed to behave elastically. This means that the state of the tissue only depends on the current loading; there is no effect from previous loading. By idealizing the tissue as an elastic material, the task of describing its behavior is reduced to a matrix of 81 stiffness constants that must be specified [4]. Since obtaining these constants is a very challenging process, additional assumptions are often made to reduce the complexity of describing the tissue behavior [5].

It is important to recognize the assumptions that are often employed to create a simple mathematical model of a tissue system. Tissue has a hierarchical structure and by choosing the scale or size of the tissue samples that are being studied, it is often possible to assume that the tissue is orthotropic, so the number of constants is reduced to 27. Then, by further restricting the scale of the sample so that the small structures in the system are randomly and uniformly distributed in the sample, the assumption of homogeneity is usually employed so that only 12 constants are needed to describe the tissue. If the scale of the tissue is picked with care, it may be appropriate to approximate the tissue as an isotropic material so that only two constants are needed to describe the tissue's response to mechanical loads. These two constants are the Lamé constants, or their technical derivatives, the Young's modulus and the Poisson's ratio.

The elastic properties of soft tissues depend on their molecular building blocks, and on the microscopic and macroscopic structural organization of these blocks [6]. The standard medical practice of soft tissue palpation is based on qualitative assessment of the low frequency stiffness of tissue. Pathological changes are generally correlated with changes in tissue stiffness as well. Many cancers, such as scirrhous carcinoma of the breast, appear as extremely hard nodules [7]. In many cases, despite the difference in stiffness, the small size of a pathological lesion and/or its location deep in the body preclude its detection and evaluation by palpation. In general, the lesion may or may not possess echogenic properties that would make it ultrasonically detectable. For example, tumors of the prostate or the breast could be invisible or barely visible in standard ultrasound examinations, yet be much harder than the embedding tissue [8]. Diffuse diseases such as cirrhosis of the liver are known to significantly increase the stiffness of the liver tissue as a whole [7], yet they may appear normal in conventional ultrasound examination. Since the echogenicity and the stiffness of tissue are generally uncorrelated, it is expected that imaging tissue stiffness or strain will provide new information that is related to pathological tissue structure. This expectation has now been confirmed [8]. In addition to pathology, we now have additional evidence that various *normal* tissue components possess consistent differences in their stiffness parameters as well. For example, in the ovine kidney, the stiffness contrast between the cortex and the medullary pyramids has recently been measured to be only about 6 dB at low strains, and strain images showing easily discernible contrast have been made [9]. This observation provides the basis for imaging the normal anatomy as well. Another observation that has been made recently is that some normal and pathological tissues may posses nonlinear stress/strain behavior. This means that their stiffnesses are a function of strain. This property may be useful in differentiating normal from abnormal tissues.

Over the past 20 years numerous investigations were conducted to characterize the mechanical properties of biological tissue systems [10–19], which have been idealized often as homogeneous, isotropic elastic materials. Much of the work has focused on bone, dental materials and vascular tissue. There are articles that discuss methods used to characterize these tissues, and there is a large volume of experimental data about the mechanical response of these tissues to various types of loadings [15,20–25]. However, there is a void in the retrievable literature regarding the mechanical properties of tissue systems tested in vivo. In fact, there is very limited information about the mechanical properties of most of the soft tissue systems that make up the body's organs. Yamada's book [19] presents a relatively broad range of data, but much of the data is derived from experiments using animal tissues and all of the information relates to uniaxial tensile rather than compressive tests of the tissue. A recent article by Krouskop et al. [26] provides compressive stiffness values for normal and pathological breast and prostate tissues in vitro.

The stiffness parameter is a function of the elastic modulus of the tissue and its geometry. It cannot be measured directly. A mechanical stimulus of some kind must be propagated into the tissue, and precision means for detecting the resulting internal tissue motions must be provided. Such means may include ultrasound, MRI or other diagnostic imaging modalities. In the last fifteen years, interest has been mounting in the ultrasonic imaging of tissue elasticity parameters. A comprehensive literature review of this field can be found in Ophir et al. [23] and in Gao et al. [15], and will not be repeated here. Tissue elasticity imaging methods based on ultrasonics fall into two main groups: (1) methods where a quasi-static compression is applied to the tissue and the resulting components of the strain tensor are estimated [22,27]; and (2) methods where a low frequency vibration is applied to the tissue and the resulting tissue behavior is inspected [21, 28–31]. In this paper, we concentrate on describing the recent progress using the first approach that we call elastography, which has been under development in our laboratory since 1989. We first present a short summary of the theory of elasticity as it pertains to the quasi-static application of loads to biological tissues. We then give some basic tissue stiffness results that demonstrate the existence of stiffness contrast among normal tissues, and between normal and pathological tissues in the breast and prostate. These data provide the continued motivation for the further development of this field. We proceed to describe the elastographic process, starting from the tissue elastic modulus distribution, progressing through various algorithms for precision time delay estimation of echoes from strained tissues, and culminating in the production of the elastogram. The use of ultrasound to acquire tissue motion information results in certain basic limitations on the attainable elastographic image parameters, which may be described by the theoretical framework known as the Strain Filter [32]. The strain filter may be used to predict and design important improvements to various elastographic image attributes, such as dynamic range expansion [33] and improvement in $\mathrm{SNR_e}$ through multiresolution processing [34]. In combination with certain Contrast-Transfer Efficiencies (CTE) inherent in the conversion of modulus to strain contrast [35,36], the strain filter formalism may be used to predict the upper-bound as well as the practically attainable Contrast-to-Noise-Ratio ($\mathrm{CNR_e}$) performance of elastography [37]. We conclude with some recent results that demonstrate that quality elastograms may be produced and interpreted under low and high elastic contrast conditions, both in vitro and in vivo.

2. Basic elasticity theory for static compressions

Materials may be classified into two groups, solids and fluids. The mechanical properties of elastic materials are expressed in terms of moduli, which relate a given applied stress to a resulting strain. Therefore, many moduli for a solid may be defined depending on the applied stress, bulk compression, torsion, shear stress, extension, etc. For a large number of solids, the measured strain is proportional to the load over a wide range of loads. This linear relationship is known as Hooke's law, which states that each of the components of the state of stress at a point is a linear function of the components of the state of strain at the same point [5]. Mathematically, this is expressed as a constitutive equation, which may be written in tensor notation as:

$$\sigma_{kl} = C_{klmn} e_{mn} \tag{1}$$

where the components C_{klmn} are elastic constants. There are a total of 81 constants corresponding to the indices, k, l, m, and n taking values equal to 1, 2, and 3. Since both the stress tensor σ_{kl} and the elasticity tensor C_{klmn} are symmetric, the number of elastic constants reduces to 27. These constants characterize a general anisotropic, linearly elastic material. Since the elastic properties of an isotropic material are independent of the orientation of the axes, the number of elastic constants is further reduced to 3 constants which may be expressed in terms of only two independent parameters known as the Lamé's constants λ and μ. These 3 constants are given by

$$C_{1122} = \lambda, \qquad C_{1111} = \lambda + 2\mu, \qquad C_{1212} = \tfrac{1}{2}(C_{1111} - C_{1122}) = \mu \tag{2}$$

The constant μ, also known as G, is referred to as the shear modulus.

The volume change rate per unit volume due to spherical stress is dependent on the bulk compressional modulus, K, related to the Lamé's constants by:

$$K = \frac{3\lambda + 2\mu}{3} \tag{3}$$

There are also two other engineering parameters commonly used to characterize the mechanical properties of solid materials: Young's modulus, E, and Poisson's ratio, ν. These are related to K and G by the following expressions:

$$K = \frac{E}{3(1-2\nu)} \quad \text{and} \tag{4a}$$

$$G = \frac{E}{2(1+\nu)} \tag{4b}$$

In general, soft tissues are anisotropic, viscoelastic and nonlinear. However, it is usually assumed that they behave as linear, elastic, isotropic materials in order to simplify the analysis. These assumptions are likely to be reasonable for small strains, rapid load application and a spatial scale that is large compared to the relative correlation length of the elastic variability in the tissue sample [26].

Soft tissues contain both solid and fluid components and therefore may have mechanical properties that fall between those of both materials [38]. The ratio G/K is close to a few tenths for solid materials, while it equals zero for liquids (i.e. liquids are incompressible and their Poisson's ratio equals 0.5 and from equation (4a), $K \to \infty$). Many soft tissues are nearly incompressible with Poisson's ratios ranging from 0.49000 to 0.4999, which make them mechanically similar to liquids. For most solids, Poisson's ratios are between 0.2 and 0.4. Note that from equation (4b) for incompressible tissues ($\nu = 0.5$), $E = 3G$. This means that there exists a simple proportionality between the shear and the Young's moduli.

The bulk modulus K may be estimated from the propagation speed of bulk compressional waves c and the material density ρ; i.e., $K \cong \rho c^2$. Since it is well known from the literature that the dynamic ranges of the speed of sound as well as the density in soft tissues are small, the dynamic range of the bulk modulus of tissues is small as well. For the purpose of ultrasonic imaging, the speed of sound in tissue is therefore assumed to be constant. Thus, the ability to create properly scaled sonograms of soft tissues is in part due to this small variability in the speed of sound. Recently, it has been shown that the shear modulus of normal and abnormal soft tissues may span more than an order of magnitude [18,26]. The graphs of ***figure 1*** summarize tissue shear modulus data obtained from different breast and prostate tissues. As can be seen, a relatively large dynamic range of the shear modulus exists in normal and abnormal breast and prostate tissues.

This relatively large dynamic range of the shear modulus is related to manual palpation methods, and responsible for the increased interest in developing new techniques for imaging information related to this modulus. It is known that the force generated by the vertical displacement of a piston into soft tissue is determined by the shear modulus [38]. To illustrate this, consider the classical solution of the force generated by the vertical displacement W of a circular piston of radius R into a semi-infinite elastic medium with elastic moduli G and K. This force is given by:

$$P = \frac{8GRW}{1 + \dfrac{G/K}{1 + G/3K}} \tag{5}$$

where the terms containing the ratio G/K vanish in soft tissues where $G \ll K$. Thus, the relationship between the force P and the displacement W is determined by the shear modulus. In other words, information from manual palpation is independent of the bulk compressional modulus K.

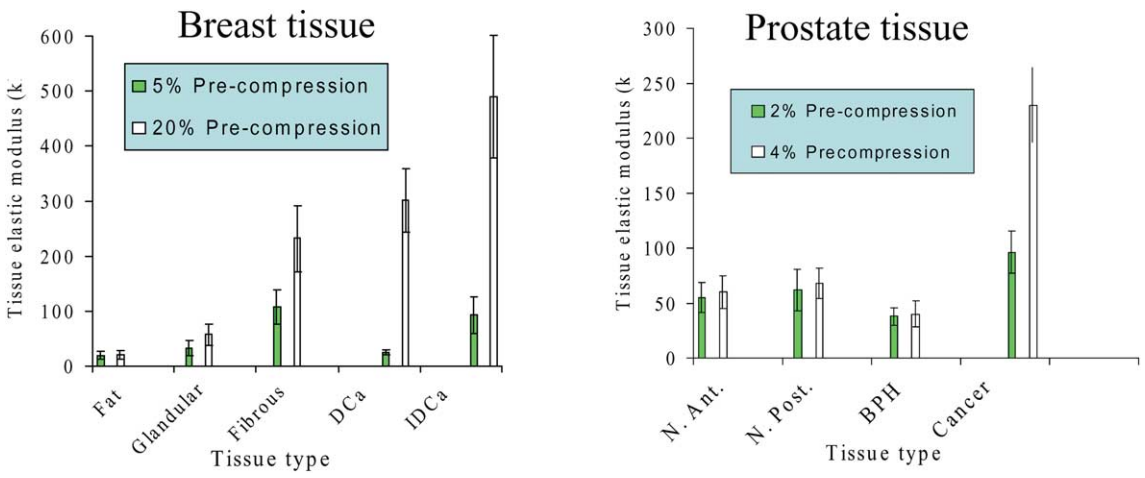

Figure 1. Tissue elastic moduli obtained from normal and abnormal breast and prostate tissues [26]. DCa = ductal carcinoma, IDCa = intraductal carcinoma, N. Ant. = anterior portion of the normal prostate, N. Post. = posterior portion of the normal prostate, BPH = benign prostatic hypertrophy.

In general, the static equilibrium of an isotropic, linear elastic material of shear modulus G, subjected to a given set of boundary conditions, is governed by the following equation:

$$\nabla p + \nabla(G\nabla u) = 0 \tag{6}$$

where u is a displacement field and p is a scalar pressure given by:

$$p = \lim_{\nabla u \to 0}[K\nabla u] \tag{7}$$

For an incompressible material, $\nabla u = 0$. Another useful set of equations describing the equilibrium-state of a linear, isotropic, elastic material is given in [18] as:

$$\begin{aligned} e_{xx} &= \frac{1}{E}\big[\sigma_{xx} - \nu(\sigma_{yy} + \sigma_{zz})\big], \qquad e_{xy} = \frac{1+\nu}{E}\sigma_{xy} \\ e_{yy} &= \frac{1}{E}\big[\sigma_{yy} - \nu(\sigma_{xy} + \sigma_{zz})\big], \qquad e_{yz} = \frac{1+\nu}{E}\sigma_{yz} \\ e_{zz} &= \frac{1}{E}\big[\sigma_{zz} - \nu(\sigma_{xx} + \sigma_{yy})\big], \qquad e_{zx} = \frac{1+\nu}{E}\sigma_{zx} \end{aligned} \tag{8}$$

where e_{xx}, e_{yy}, e_{zz}, etc., are the orthogonal strain tensor components and $\sigma_{xx}, \sigma_{yy}, \sigma_{zz}$, etc., are the corresponding orthogonal stress tensor components. In principle, for a given Poisson's ratio, any equation relating a given strain distribution to a corresponding set of stress distributions may be used to estimate the corresponding Young's modulus distribution. For example, as shown by *figure 2*, in the case of a plane-strain state problem, the modulus distribution may be obtained using the following relation:

$$E = \frac{(1+\nu)((1-\nu)\sigma_{xx} - \nu\sigma_{yy})}{e_{xx}} \tag{9}$$

In general, only the strain distribution may be *directly* estimated in practice. However, this strain distribution is not an intrinsic tissue property. It is dependent on both internal and external boundary

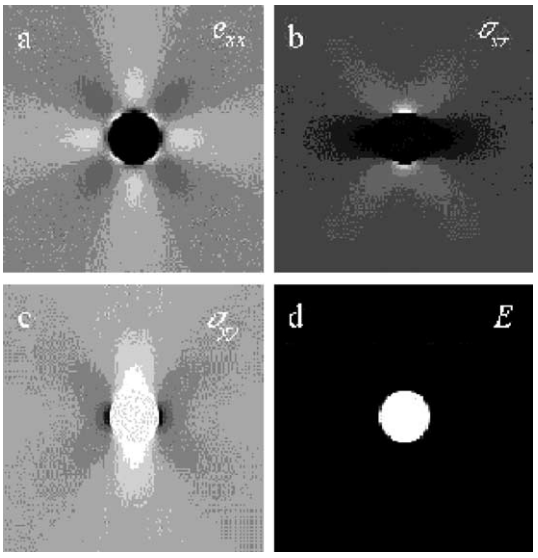

Figure 2. Illustration of modulus distribution estimation from orthogonal strain and stress distributions using equation (9). The Poisson's ratio is assumed to be 0.5.

conditions, as well as on the distribution of shear moduli in the tissue. The external boundary conditions depend on the shape and relative size of the compressor as well as on the degree of friction between the contact surfaces. The shape and type of the tissue components determine the internal boundary conditions. Therefore, a map of the strain distribution in tissue reveals not only information about tissue shear modulus distributions, but also about tissue connectivity (interfaces between tissue components) and other geometrical considerations. Alternatively, the map is designated as a 'stiffness' distribution, which includes the effects of the modulus and the geometry. An incorrect interpretation of the stiffness distribution as being the shear modulus distribution may result in some known artifacts. However we have previously demonstrated [9] that for low modulus contrast and simplifying geometrical boundary conditions, the stiffness distribution may be a relatively good representation of the underlying modulus distribution.

3. The elastographic process

When a constant uniaxial load deforms an elastic medium, all points in the medium experience a resulting level of longitudinal strain whose principal components are along the axis of compression. If one or more of the tissue elements has a different stiffness parameter than the others, the level of strain in that element will generally be higher or lower; a stiffer tissue element will generally experience less strain than a softer one. The longitudinal axial strain is estimated in one dimension from the analysis of ultrasonic signals obtained from standard diagnostic ultrasound equipment. This is accomplished by acquiring a set of digitized radio-frequency (RF) echo lines from the tissue region of interest; compressing the tissue with the ultrasonic transducer (or with a transducer/compressor combination) along the ultrasonic radiation axis by a small amount (generally about 1% or less of the tissue depth), and; acquiring a second, post-compression set of echo lines from the same region of interest. Congruent echo lines are then subdivided into small temporal windows that are compared pair-wise by using one of a variety of possible time delay estimation techniques such as cross correlation, from which the change in arrival time of the echoes before and after compression can be estimated. Due to the small magnitude of the applied compression, there are only small distortions of the echo lines, and the changes in arrival times are also small. The local longitudinal strain is estimated as:

$$e_{11,\mathrm{local}} = \frac{(t_{1b} - t_{1a}) - (t_{2b} - t_{2a})}{t_{1b} - t_{1a}} \tag{10}$$

where t_{1a} is the arrival time of the pre-compression echo from the proximal window; t_{1b} is the arrival time of the pre-compression echo from the distal window; t_{2a} is the arrival time of the post-compression echo from the proximal window; and t_{2b} is the arrival time of the post-compression echo from the distal window. The windows are usually translated in small overlapping steps along the temporal axis of the echo line, and the calculation is repeated for all depths. The fundamental assumption made is that speckle motion adequately represents the underlying tissue motion for small uniaxial compressions. This assumption appears to be reasonable as long as the distributions of the scatterers before and after compression remain highly correlated. We have shown recently [39] that the lateral motion of the scatterers due to tissue compression may also be estimated with high precision using novel interpolation techniques operating on signals obtained from overlapped beams. This allows the generation of elastograms that depict the lateral components of the strain tensor, re-correlation of the signals prior to the computation of the axial strains, resulting in better image quality, and/or the generation of elastograms depicting the local ratios of the lateral-to-axial strains (effectively, the Poisson's ratio).

It is important to emphasize that elastography is a method that can ultimately generate several new kinds of images. As such, all the properties of elastograms are different from the familiar properties of sonograms. While sonograms convey information related to the local acoustic backscatter energy from tissue components, elastograms relate to its local strains, Young's moduli or Poisson's ratio. In general, these elasticity parameters are not directly correlated with sonographic parameters, i.e., elastography conveys new information about internal tissue structure and behavior under load that is not otherwise obtainable.

The general process of creating elastograms, beginning with the modulus distribution in tissue and ending with a corresponding axial strain elastogram, is shown in *figure 3*, showing a block diagram of the process. The first block of the process corresponds to the intrinsic tissue modulus distribution. The intermediate block corresponds to the ideal strain distribution in the target that relates to the behavior of the target under a compressive load. The transformation from modulus contrast to strain contrast involves a certain loss of efficiency. This may be computed for simple targets by the Contrast-Transfer Efficiency (CTE) function. The output image corresponds to the strain (axial and/or lateral) image (elastogram), which is a corrupted (noisy) version of the ideal strain image. The noise and contrast properties of the elastogram are computed from the Strain Filter (SF), which takes into account the engineering and acoustical parameters that limit

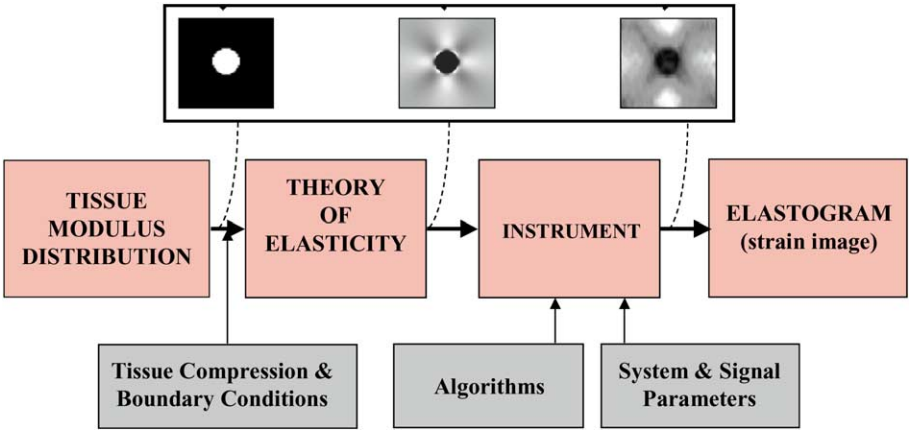

Figure 3. The general block diagram process of creating an elastogram. The modulus contrast distribution is converted to a strain contrast distribution using the Contrast-Transfer Efficiency (CTE). The ideal strain contrast distribution is estimated from ultrasonic strain estimates by the ultrasound system whose performance is constrained by the Strain Filter (SF) for particular technical and algorithmic parameters. The result is an estimated strain contrast distribution (elastogram).

the ultimate quality of the attainable elastogram. The block describing the Strain Filter [32] embodies the selective filtering of the tissue strains by the ultrasound system and signal processing parameters. The SF predicts a finite dynamic range and respective elastographic signal-to-noise ratio ($\mathrm{SNR_e}$) at a given resolution in the elastogram, limited by noise and/or decorrelation. The contributions of the signal processing and ultrasound system parameters and other algorithms are indicated as inputs into the SF. Combining the CTE and the SF formulations leads to the description of the elastographic contrast-to-noise ratio ($\mathrm{CNR_e}$) in the elastogram. All these blocks are described later in this article. A complete description may be found in Ophir et al. [39].

4. Contrast-Transfer Efficiency (CTE)

Using ultrasonic techniques, it is only possible to measure some of the local longitudinal components of the strain tensor in the tissue. The local components of the stress tensor remain unknown. The strain elastogram is all that is available to represent the distribution of tissue elastic moduli, if this is indeed what is desired. The CTE is defined as the ratio of the observed (axial) strain contrast measured from the strain elastogram and the underlying true modulus contrast. Expressed in decibels, it is given by:

$$\mathrm{CTE(dB)} = \left|C_o(\mathrm{dB})\right| - \left|C_t(\mathrm{dB})\right| \tag{11}$$

where the magnitude is used in order to have CTE normalized to the zero dB level; i.e. the maximum efficiency is reached at 0 dB for both hard and soft inclusions. This fundamental property of elastography has been verified by finite-element simulations and was also corroborated theoretically, using models of simple geometry [35,36]. *Figure 4* shows the behavior of the CTE parameter over an 80 dB dynamic range of modulus contrast as measured from simulated data and as predicted using an analytical model. It is clear from the figure that, for low modulus contrast levels (a high level of target modulus homogeneity), the elastographic strain contrast is relatively close to the modulus contrast ($\mathrm{CTE} \approx 1$ or 0 dB). This is a very important observation, since it suggests that, for low modulus contrast tissues, the simply computed axial strain elastogram itself is very similar to the inverse of the true modulus elastogram. This expected result has been verified experimentally using ex-vivo ovine kidneys and phantoms [9,46]. Hard inclusions have a relatively high level of contrast-transfer efficiency. However, soft inclusions that are completely surrounded by harder background material have low contrast-transfer efficiency, and thus may not be well visualized by elastography. The reason for this limitation lies in the fact that, due to the incompressible nature of many soft tissues (Poisson's ratio ~ 0.5), the soft inclusion will be constrained so that it will not be able to deform

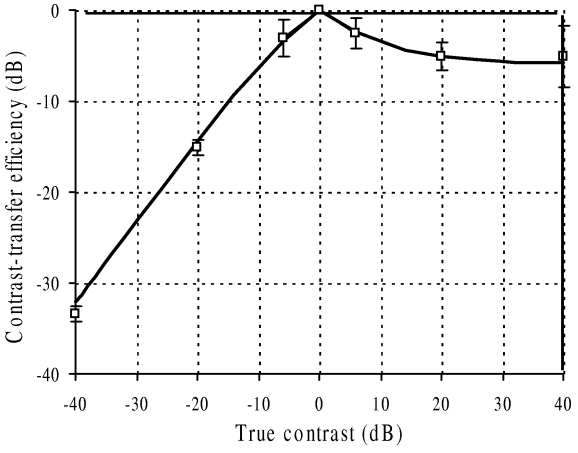

Figure 4. The behavior of the contrast-transfer efficiency function for a plane-strain-state circular inclusion. Note that the strain contrast is close to the modulus contrast (efficiency $= 1$ or 0 dB) for low modulus contrast lesions. Note also that the function is asymmetric, demonstrating high efficiency for stiff inclusions, and low efficiency for soft inclusions.

under load as it might otherwise do without constraints. It will thus assume instead new elastic properties that are closer to those of the surrounding stiffer material.

5. Time delay estimation (TDE) in strained tissues

Time delay is a very important parameter in elastography. Tissue strain is typically estimated from the axial gradient of tissue displacements. The local tissue displacements are estimated from the time delays of gated pre- and post-compression echo signals. Time delays are generally estimated from the location of the peak of the crosscorrelation function between the pre- and post-compression echo signals.

The quality of elastograms is highly dependent on the quality of the TDE procedure. TDE in elastography is mainly corrupted by two factors. First, random noise introduces errors in the TDE. Second, tissue needs to be compressed to produce elastograms. The very same compression of the tissue distorts the post-compression signal such that it is no longer an exact delayed version of the pre-compression signal. This decorrelation increases with increasing strain and is independent of the signal-to-noise ratio in the echo signals. Any phenomenon (such as lateral and elevational motions) that degrades the precision of the time-delay estimates will also degrade the strain estimates, thus introducing additional noise into the elastogram.

Echo signal decorrelation is one of the major limiting factors in strain estimation and imaging. For small strains, it has been shown that temporal stretching of the post-compression signal (or temporal compression of the pre-compression signal) by the appropriate factor can almost entirely compensate for such axial decorrelation in a mechanically homogeneous medium. When the post-compression echo signal is stretched, it in effect realigns all the scatterers within the correlation window. Global uniform stretching was found to significantly improve the elastographic signal-to-noise ratio ($\mathrm{SNR_e}$) and expand the strain dynamic range in elastograms [40,41]. Moreover, this step is computationally simple. Thus, a global uniform stretching of the post-compression echo signal prior to the displacement estimation is highly advisable. In low contrast targets and/or low strains, this is a very efficient displacement estimator. In these situations, it produces quality elastograms without significantly adding to the computational load. However, in high contrast targets, there will be significant over-stretching in the areas of low strains, which by itself can significantly degrade elastograms in these areas. For these situations, an adaptive axial stretching algorithm [42] may be necessary. Axial stretching is mandatory in the presence of large strains; otherwise the elastograms become so noisy that they are practically useless. Axial stretching also enhances the dynamic range of elastography. It must be remembered that axial stretching can only recover most of the decorrelation suffered due to scatterer motion in the axial direction; decorrelation due to lateral and elevational motions, as well as other sources of decorrelation, cannot be compensated this way. Konofagou and Ophir [43] have demonstrated that decorrelation due to lateral motion may be compensated with high accuracy by using a phase sensitive signal interpolation technique. This technique, when applied alternately with axial stretching, was shown to result in large improvements in elastographic image quality. A deconvolution filtering approach may be useful in reducing the remaining decorrelation that results from the unintended stretching of the transducer point-spread function (PSF) when the post-compression signal is stretched [44].

6. The Strain Filter (SF)

The SF [32] describes the relationship among the resolution, dynamic range ($\mathrm{DR_e}$), sensitivity ($S_{\min}$) and elastographic $\mathrm{SNR_e}$ (see *figure 12*), and may be plotted as a graph of the upper bound of the $\mathrm{SNR_e}$ vs. the strain experienced by the tissue, for a given elastographic axial resolution (as defined by the data window length and overlap). The SF is a statistical upper bound of the transfer characteristic that describes the relationship between actual tissue strains and the corresponding strain estimates depicted on the elastogram. It describes the filtering process in the strain domain, which allows quality elastographic depiction of only a limited range of strains from tissue. This limited range of strains is due to the limitations of the ultrasound system and of the signal processing parameters and algorithms. The SF is obtainable as the ratio between

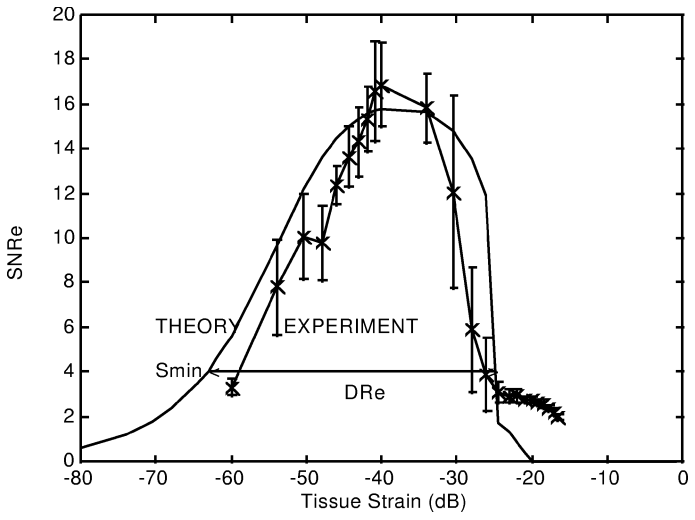

(a)

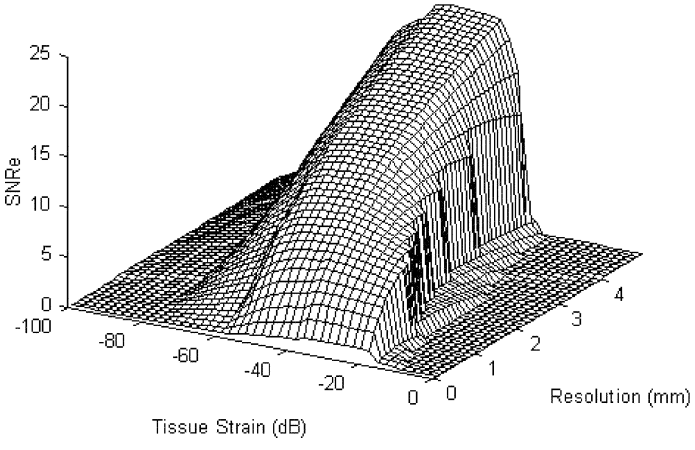

(b)

Figure 5. Typical appearance of the strain filter. The parameter Smin = the sensitivity of the strain filter; the parameter DRe = the dynamic range of the strain filter. (a) Theoretical and experimental strain filter at a fixed resolution (0 dB refers to 100% strain); (b) three-dimensional appearance of the theoretical strain filter showing the value of $\mathrm{SNR_e}$ vs. strain and resolution. Observe that $\mathrm{SNR_e}$ exhibits a maximum over a defined range of strains, and that the value of $\mathrm{SNR_e}$ trades-off against axial resolution at all strain levels.

the mean strain estimate and the appropriate lower bound on its standard deviation. The SF may be further de-rated due to effects such as axially non-stationary tissue attenuation, and laterally non-stationary speckle decorrelation due to undesired lateral tissue motion. The SF is based on well-known lower bounds on the TDE variance, presented in the literature. The low-strain behavior of the SF is determined by the variance as computed from the Cramér-Rao Lower Bound (CRLB) (modified for partially correlated signals). The high-strain behavior of the SF is determined by the rate of decorrelation of a pair of congruent signals due to tissue distortion as shown in *figure 5*. *Figure 5* illustrates the general appearance of the SF, demonstrating the tradeoffs among $\mathrm{SNR_e}$ and resolution for all strains. An important extension to the SF is its combination with the CTE formalism to produce elastographic Contrast-to- Noise Ratio ($\mathrm{CNR_e}$) vs. strain curves. This allows the description of the $\mathrm{CNR_e}$ of simple elastic inclusions or layers in terms of both the mechanical strain contrast limitations in the target, and the noise properties of the apparatus.

6.1. Theoretical framework

A parameter that quantitatively measures the noise performance of the strain estimate is the $\mathrm{SNR_e}$, defined by:

$$\mathrm{SNR_e} = m_\mathrm{s}/\sigma_\mathrm{s} \tag{12}$$

Here m_s denotes the statistical mean strain estimate and σ_s denotes the standard deviation for the strain noise estimated from the elastogram. When the statistical mean value of the strain is replaced by the ideal tissue strain, and the minimum standard deviation is replaced by the theoretical lower bound on the standard deviation, we obtain a function representing the upper bound on the $\mathrm{SNR_e}$, referred to as the Strain Filter [32]:

$$\mathrm{SNR_e^{UB}} = \frac{s_t}{\sigma(\hat{s})_{\mathrm{ZZLB},\rho}} \tag{13}$$

where s_t is the tissue strain, and $\sigma(\hat{s})_{\mathrm{ZZLB},\rho}$ is the modified Ziv–Zakai lower bound (ZZLB) on the standard deviation of the strain estimator. The ZZLB provides the tightest lower bound for the displacement estimator. The modified ZZLB expression for the strain estimation variance is complicated, and is not reproduced here.

6.2. Nonstationarity of the strain filter

Estimation of tissue strains is inherently a nonstationary process, since the pre- and post-compression RF echo signals are jointly nonstationary (due to signal deformation caused by straining tissue). However, the pre- and post-compression signals can be approximated to be jointly stationary, if the tissue strain is estimated using small windowed data segments in conjunction with temporal stretching of the post-compression signal. Frequency dependent attenuation adds additional (axial) nonstationarity into the strain estimation process vs. depth [45], while lateral and elevational signal decorrelation introduce nonstationarities in the strain estimation process along the lateral and elevational directions, respectively [46]. The SF can predict the effect of these nonstationarities on the elastogram. For example, The effect of lateral decorrelation contributes predominantly to the nonstationary variation in the $\mathrm{SNR_e}$. Both the $\mathrm{SNR_e}$ and the dynamic range are reduced with an increase in lateral decorrelation. As long as any stationary or nonstationary noise source can be described, its effect may be incorporated into the strain filter formalism, resulting in a more realistic, *derated* strain filter. An example of a derated strain filter is shown in *figure 6*.

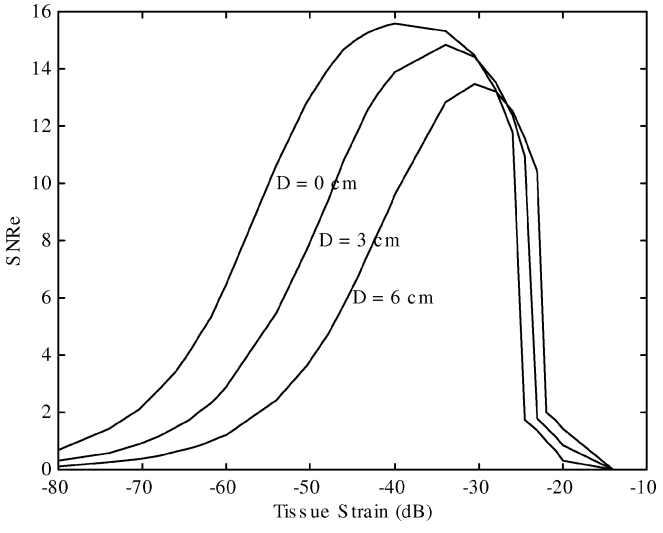

Figure 6. Example of a typical theoretical strain filter derated for typical attenuation in soft tissues. The symbol D refers to the depth in tissue. Observe that the strain filter is nonstationary, and that the strain dynamic range is reduced as a function of depth in the tissue.

6.3. Contrast-to-noise ratio in elastography

The contrast-to-noise ratio ($\mathrm{CNR_e}$) in elastography is an important quantity that is related to the detectability of a lesion. The properties of the ultrasound imaging system and signal processing algorithms described by the SF can be combined with the elastic contrast properties (CTE) of tissues with simple geometry, enabling prediction of the elastographic contrast-to-noise ratio ($\mathrm{CNR_e}$) parameter. This combined theoretical model enables prediction of the elastographic $\mathrm{CNR_e}$ for simple geometry such as layered (1D model) or circular lesions (2D model) embedded in a uniformly elastic background. An upper bound on the $\mathrm{CNR_e}$ may be obtained using the Fisher discriminant statistic, viz.:

$$\mathrm{CNR_e} = \frac{2(s_1 - s_2)^2}{(\sigma_{s1}^2 + \sigma_{s2}^2)} \tag{14}$$

The $\mathrm{CNR_e}$ for specific geometries that possess an analytic or experimental CTE description can be obtained [37] by substituting the strains obtained using the elasticity model and their respective variances from the SF into equation (14).

Figure 7 illustrates the general appearance of the upper bound on the $\mathrm{CNR_e}$, demonstrating the tradeoffs among $\mathrm{CNR_e}$ and modulus contrast for all applied strains. Note from *figure 7* and equation (14) that the highest values of the $\mathrm{CNR_e}$ are obtained where two conditions are satisfied; firstly, the differences in mean strain values must be large, and secondly the sum of the variances of the strain estimates should be small. The improvement of the $\mathrm{CNR_e}$ at low modulus contrasts is primarily due to the small strain variances, while at high modulus contrasts the improvement in the $\mathrm{CNR_e}$ is due to the large difference in the mean strains. Note from the 3D visualization of the $\mathrm{CNR_e}$ curves in *figure 7*, that when the differences in the mean strain values are small (in the region around the middle of the graph at low contrasts), the $\mathrm{CNR_e}$ value obtained is close to zero. In addition, the regions with large strains (corresponding to large variances in the strain estimate due to signal decorrelation) also contribute to low $\mathrm{CNR_e}$ values. Knowledge of the theoretical upper bound on the $\mathrm{CNR_e}$ in elastography is crucial for determining the ability to discriminate between different regions in the elastograms. The CTE for the elasticity models and the elastographic noise characterized by the SF determine the $\mathrm{CNR_e}$ in elastography. The 3D visualization of the $\mathrm{CNR_e}$ curves illustrate the strain dependence of the elastographic $\mathrm{CNR_e}$. The 3D plot provides a means of maximizing the $\mathrm{CNR_e}$ in the elastogram for the given ultrasound system and signal processing parameters.

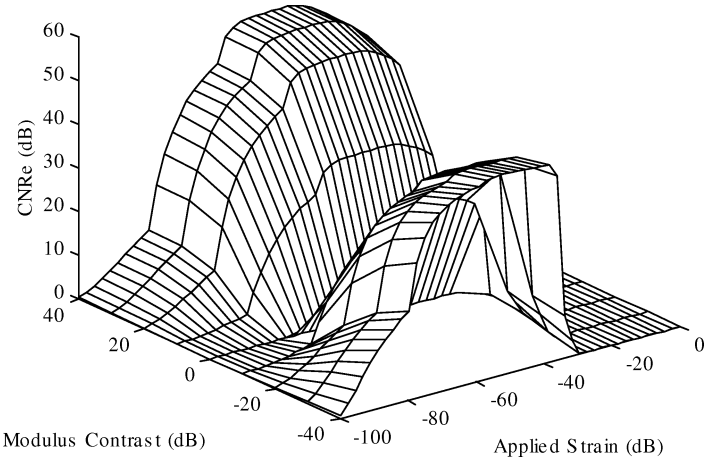

Figure 7. A typical upper bound on the elastographic Contrast-to-Noise ratio ($\mathrm{CNR_e}$) as a function of modulus contrast and strain. This function is obtainable by combining the CTE and SF formalisms.

6.4. Resolution in elastography

It has recently been demonstrated (Righetti et al., Axial resolution in elastography, submitted to Ultrasound Med. Biol.) that the upper bound on the attainable elastographic axial resolution is proportional to $Q\lambda$, where Q is the quality factor of the transducer, and λ is the ultrasonic wavelength. The constant of proportionality depends on the exact definition that is used for the axial resolution, but is generally a number between 1 and 2. This means that the sonographic and elastographic axial resolutions are of the same functional form and are of similar magnitude. Equivalently, the upper bound on the axial resolution is inversely proportional to the absolute bandwidth of the ultrasonic pulse. This limit is not always achieved [47] due to noise considerations. This is a similar limit to the one encountered in sonography, which means that comparisons between the sonograms and elastograms may be made at the same scale. The practically attainable resolution for a given system, however, is limited by the choice of window size and overlap. This also bodes well for the feasibility of micro-elastographic imaging at high frequencies. The lateral resolution of elastography has not been investigated in detail, but it is thought to be strongly related to the beamwidth of the transducer.

7. Applications of elastography

In principle, elastography may be applied to any tissue system that is accessible ultrasonically and which can be subjected to a small static (or dynamic) compression. The compression may be applied externally or internally. Any physiological phenomenon, such as pulsating arteries or respiration, may be used as a source of tissue compression. So far, elastography has been applied in vivo to breast, prostate and vascular imaging. Several in vitro studies demonstrated the potential of elastography in imaging normal anatomy. Elastography has also demonstrated potential usefulness for monitoring thermal therapy. In this section, a summary of some of these applications is presented.

Figure 8 shows that the normal anatomy of ovine kidney can be clearly demonstrated by elastographic imaging. As can be seen from *figure 9*, the strain contrast is nearly equivalent to the modulus contrast in

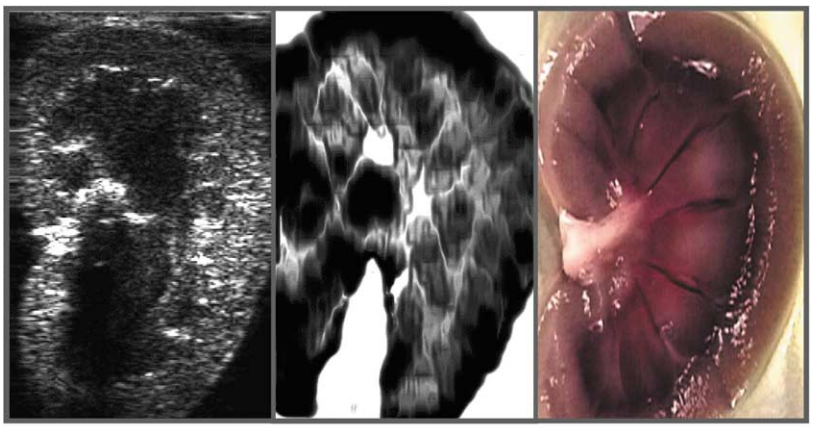

Figure 8. From left to right, longitudinal sonogram, elastogram and gross pathological specimen from an ovine kidney in vitro. The elastogram demonstrates structures that are consistent with a stiff (black) renal cortex and medullary pyramids (of which at least seven are seen), softer (white) columns of Bertin and very soft fatty areas at the base of the columns in the renal sinus. Areas of sonographic echo dropouts outside the kidney and in the acoustically shadowed areas distal to the renal sinus are intentionally blanked in the elastogram. Note that the renal sinus is hypoechoic and is not well visualized on the sonogram [9].

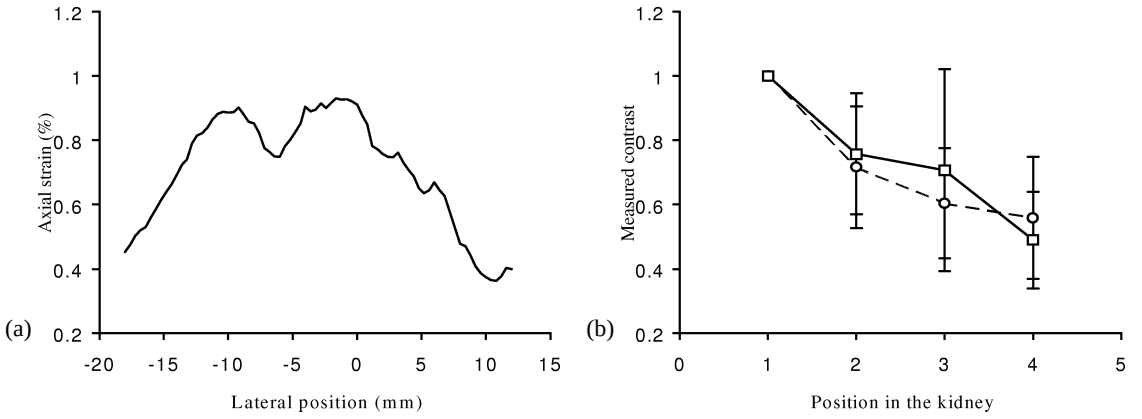

Figure 9. (a) Strain profile across the ovine kidney in vitro. Note symmetry of strain. (b) Modulus contrast (measured with an Instron testing machine on a sample) and strain contrast variation (measured from the elastogram) from the renal cortex to the medulla. Note that within the error bars, the strain contrast is equivalent to the modulus contrast. Note that this observation is consistent with the high contrast transfer efficiency predicted by the CTE function for low-modulus contrast cases [9].

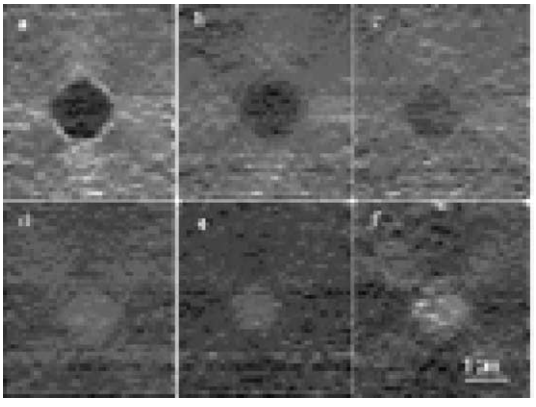

Figure 10. Elastograms obtained from six phantoms embedding cylindrical inclusions. The inclusion background contrast is 6.8, 4.2, 2.8, -2.3, -3, and -7.5 dB for the elastograms a, b, c, d, e, f, respectively [48]. The horizontal white line at the bottom right corner represents 1 cm.

cases of tissues that have a narrow dynamic range of elastic moduli, such as the normal ovine kidney. This is predicted by the CTE function.

Figure 10 shows six elastograms obtained from different low contrast phantoms. These phantoms were made from a mixture of gelatin and agar powder. A fixed agar concentration was used to elicit acoustic scattering. Various stiffness contrasts were obtained by changing the gelatin concentration. The inclusion/background contrast of the stiffest inclusion was 6.8 dB and the contrast of the softest inclusion was -7.5 dB. The elastograms are clearly capable of depicting contrast levels that were as low as 2.8 dB and -2.3 dB with relatively high contrast to noise ratio. This is predicted by the $\mathrm{CNR_e}$ function.

A typical example of the elastographic visualization of a canine prostate in vitro is shown in *figure 11*. In the elastograms, the white (stiff) rim, depicted in both the transverse and sagittal views and in each slice, corresponds to the outer gland that surrounds a softer (gray) inner gland, which is consistently demonstrated in each slice. In the center of the prostate, the verumontanum is elastographically demonstrated as a small stiff (white) ridge along the urethra. The lumen of the urethra is depicted as a soft (black) inverted "V" or "U" shaped area. By comparison, the companion sonograms do not provide a clear visualization of the aforementioned anatomical structures in the prostate.

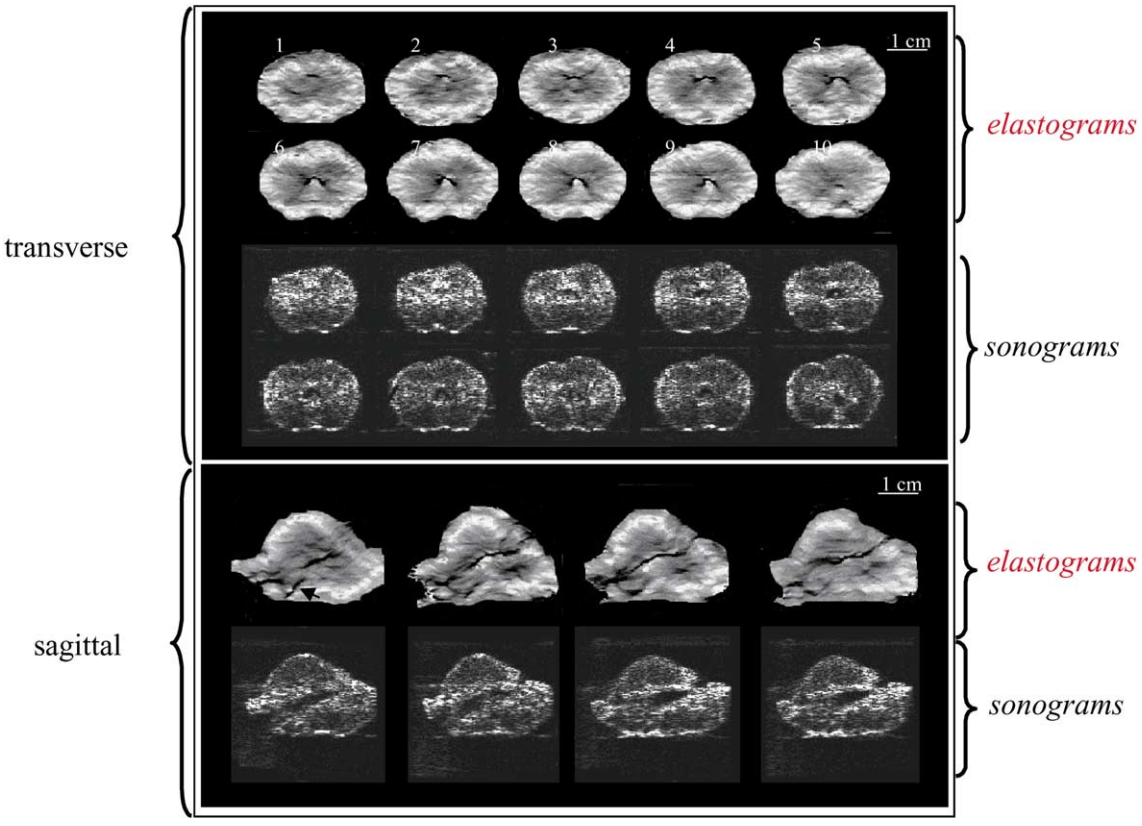

Figure 11. Matching elastograms and sonograms obtained from 1 mm equally spaced parallel transverse and sagittal cross-sections of a typical canine prostate at 5 MHz. The prostate size is approximately $3 \times 3 \times 3$ cm^3. The elastograms are displayed using a reversed gray-scale map where white means stiff and black means soft [49]. Note the clear depiction of the urethra, consistently stiffer outer gland and softer inner gland, the soft acini and the stiff verumontanum in the corresponding elastograms.

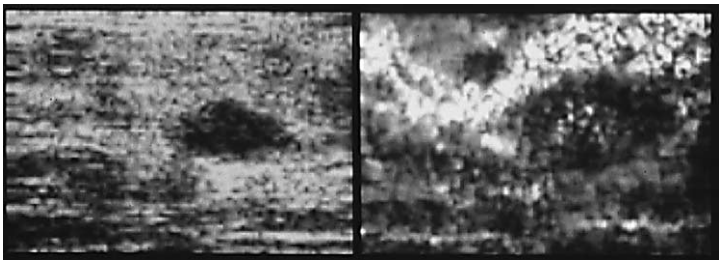

Figure 12. From left to right, matching sonogram and elastogram of breast carcinomas obtained in vivo in the erect position at 5 MHz [23]. Note the demonstration of two hard nodules and the torturous soft subcutaneous fat layer on the elastogram. Note also that the sonogram demonstrates only one hypoechoic nodule and that a size discrepancy exists between the sonographic and elastographic appearance of the large nodule (presumably due to desmoplasia).

The first in vivo application of elastography was to the imaging of the breast and skeletal muscle [25]. An example of the visualization of breast carcinoma is given in *figure 12*. Both the B-scan and the corresponding elastogram show a large lesion at 3 o'clock. The size of this lesion on the elastogram is

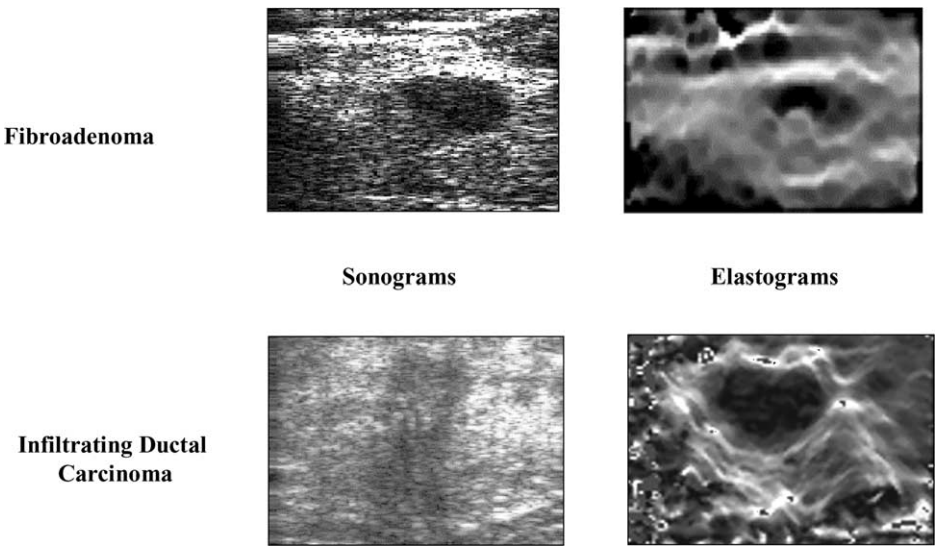

Figure 13. Sonogram and elastogram pairs from fibroadenoma and carcinoma of the breast in vivo at 5 MHz. Observe the clear depiction of the carcinoma on the elastogram (including the distal margins), as well as the size discrepancy between the sonographic and elastographic appearance of the carcinoma.

larger compared to its size on the corresponding sonogram. The elastogram also depicts a second, much smaller lesion at 11 o'clock, which is not demonstrated in the sonogram. Both lesions were pathologically confirmed. Further work has demonstrated that, unlike benign breast tumors, cancers were consistently larger on the elastogram compared to their corresponding size on the sonogram. This size discrepancy was hypothesized to be associated with desmoplasia surrounding the cancerous lesion.

The earliest breast images were obtained in a sitting position, which limited the number of accessible cancers for elastographic imaging. More recently, breast elastograms were obtained in the supine position, which allowed the imaging of cancers that were close to the chest wall. An example of elastograms and a corresponding sonograms of a fibroadenoma and a carcinoma obtained in the supine position is shown in *figure 13*. Observe the size discrepancy between the sonographic and elastographic appearance of the carcinoma unlike in the case of the fibroadenoma.

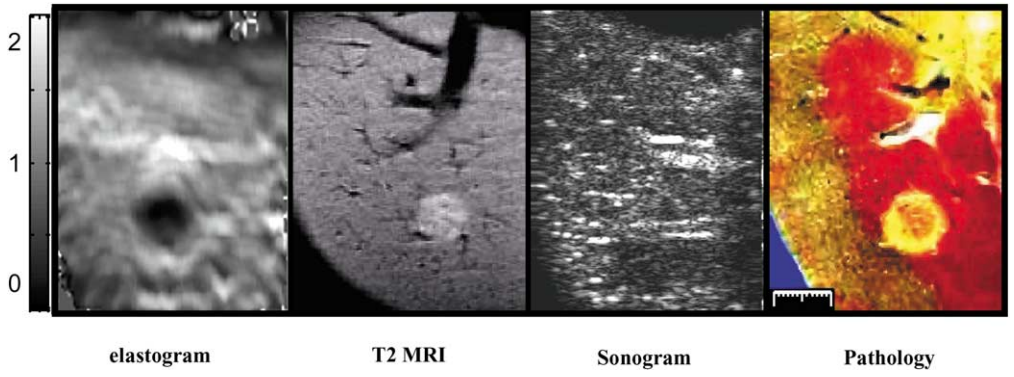

Figure 14. From left to right: elastogram, coronal T2-weighted-MR image, sonogram and gross (stained) pathological specimen of a HIFU lesion induced in a canine liver in vitro. Note that the sonogram does not demonstrate the HIFU lesion [50].

Elastography has shown promise for monitoring tissue stiffening due to thermal ablative procedures. An example of the visualization of High Intensity Focused Ultrasound (HIFU) lesion induced in a canine liver in vitro is shown in *figure 14*, where the lesion appears as a hard nodule. It is noted that the sonogram does not demonstrate the lesion.

8. Summary and conclusions

The assumption driving the development of elastography has been that significant soft tissue modulus contrast exists, especially between normal and abnormal tissues. Perhaps not surprisingly, it has been recently demonstrated that modulus contrast exists not only between normal and pathological tissues, but to a lesser degree also between and within normal tissues. The existence of this lower contrast could be ascertained only following recent vast improvements in the elastographic image quality due to a better understanding of the theory of elastographic image formation that led to the development of better algorithms, such as adaptive signal stretching, and lateral motion re-correlation. These observations, together with some initial clinical observations showing the ability of elastography to detect and characterize sonographically occult breast cancers, are providing the catalyst for continuing the vigorous development and application of elastographic methods to medical imaging problems.

Proper strain estimation strategies are critical to the practice of elastography. Early strain estimators were based on the calculation of the gradient of estimated displacements. The gradient operation is known for its noise-enhancing property. A least-squares strain estimator for elastography has been proposed [51], which was shown to improve elastographic signal-to-noise ratio (SNRe). Alam et al. [42] proposed the adaptive stretching algorithm, which iteratively varies the local temporal stretching factor to directly estimate strain. While coherent (cross-correlation) methods used in conventional elastography generally have the advantage of being highly accurate and precise, even relatively minor undesired motions can produce sufficient signal decorrelation to cause significant degradation of the elastogram. On the other hand, incoherent spectral estimators are moderately less precise but far more robust. We have observed that local strain causes a scaling of the RF echo spectra that is directly proportional to strain. This frequency-scaling can be measured via the spectral centroid shift [52] or spectral cross-correlation [53]. Spectral estimators [52,53], and adaptive stretching techniques [41] estimate strain directly (i.e., without using noise-amplifying gradient operators) within a single estimation window. In spectral adaptive stretching [54], the principles of adaptive stretching have been applied in the spectral domain, thus combining their advantages. A novel rigid-body motion estimator has been proposed that does not directly estimate strain, but provides a map of relative stiffness in tissues [54]. This method provides acceptable performance when the applied compression is large or significant non-axial component of motion is present, causing conventional methods to fail. To estimate strain in harsh environments such as in hand-held scanning situations, it may be necessary to develop even more sophisticated strain estimation strategies in the future.

The estimation and imaging of tissue strains is by definition a three-dimensional problem. When the tissue is compressed, the near incompressibility of most soft tissues means that strain tensor components are generated in all directions simultaneously. Until recently, workers in the field had assumed that single-view ultrasonic methods could not be used for precision lateral displacement and strain estimates. As a result, they were essentially limited to displacement and strain estimations in the axial direction only. It has recently been demonstrated [43] that it is in fact possible to make precision estimations of lateral displacements and produce images of lateral strain and Poisson's ratio distributions in tissues, if proper overlap between adjacent ultrasonic beams is maintained. With 2D arrays, or by using a 1D array and measuring the residual elevational decorrelation after correcting for the other two components, it should be possible to precisely estimate all three longitudinal components of the strain tensor in tissues using clinical array scanners. Poisson elastograms may be important in the imaging of poroelastic, edematous and viscoelastic tissues [43].

Given the fortunate existence of significant modulus contrast in many normal and abnormal tissues, and the ability to estimate some of the components of the strain tensor, the noise performance of these estimations becomes the important parameter that dictates the achievable contrast-to noise ratio in elastograms. The strain filter framework has been developed to describe the tradeoffs among all the technical parameters of the ultrasound instrumentation in terms of their influence on the elastographic image parameters. Using this formalism, it has been demonstrated that axial-elastograms with high $\mathrm{CNR_e}$, wide strain dynamic range and good strain sensitivity can be achieved at resolutions that are on the order of the ultrasonic pulse width. These can be further improved by correcting for lateral displacements and axial distortions. Given further that axial or lateral elastograms display the distributions of the respective strains and not of the moduli, a contrast-transfer-efficiency (CTE) metric has been defined and calculated. This metric adds a description based on elasticity theory of the efficiency with which actual modulus contrast is converted to elastographic strain contrast under known conditions. We have shown that for low contrast situations such as in the normal ovine kidney, the strain image is a reasonable representation of the actual inverse modulus image. We have also shown that elastography holds promise in the evaluation of breast masses in vivo. Based on the progress described in this article, it is accurate to say that at this point the fundamental aspects of elastographic imaging are reasonably well understood and can be theoretically predicted and practically analyzed.

Many interesting challenges remain in the development of this new field. In principle, it should be possible to generate elastograms in real-time, perhaps by reducing the cross-correlation computations to 1-bit hardware operations, which have been shown to be effective, or by using fast Digital Signal Processing (DSP) chips. The ultimate limitation on speed is the speed of sound and the speed of propagation of the elastic wave in tissue. The current need for a transducer holding apparatus is another major limitation. This could be overcome by estimating the unpredictable coarse and fine lateral and elevational displacements encountered in hand-held elastography, and correcting the axial-elastogram appropriately so that quality images can be generated. This approach is powerful in that it is able to remove severe decorrelation noise that is introduced when the local strain filter at any point in the image enters the Barankin bound due to excessive and/or undesired motion. Another solution may involve the use of incoherent strain estimators that are less sensitive to jitter and other undesired motions. A ‘stress meter’ in the form of an elastic layer attached to the transducer or the target may be used in conjunction with a hand-held device to allow automatic nonstationary image calibration for uneven compressions. The optimal elastographic protocols that are to be followed when imaging certain tissues are as yet unknown. These include the amount of pre-compression, the applied imaging compression, the number of sonographic frames and the (adaptive) algorithm(s) to be used for image optimization, and the relationship of these protocols to the specific elastic properties (such as contrast and nonlinear stress/strain behavior) of most tissues. While elastographic artifacts are fairly well understood, their possibly ambiguous role as detractors or facilitators of lesion detection and/or diagnosis remains unknown. Related techniques, such as high frequency, high-resolution methods applied intravascularly may also develop as useful adjuncts to the current sonographic methods. Another important area that could greatly benefit from the incorporation of elastographic techniques is the area of thermal or cryogenic tissue ablation monitoring. It is known that standard sonographic techniques are not well suited for monitoring such procedures due to their poor precision. We have recently shown that elastography offers high precision in monitoring laser and HIFU applications [50].

In conclusion, we believe that while elastography has progressed rapidly in the past several years, much progress has yet to be made in order for elastography to become a viable clinical and investigational tool. Even at this early stage, however, it is evident that there exists a fortunate set of favorable biological, mechanical and acoustical circumstances that, when combined, will inevitably allow the attainment of this goal.

Acknowledgements. This work was supported by the National Cancer Institute (USA) Program Project Grant P01-CA64597 to the Ultrasonics Laboratory at the University of Texas Medical School in Houston.

References

[1] Carton R.W., Clark J.W., Barron A., Dainauskas J., Estimation of tissue elasticity of the lung, J. Appl. Physiol. 19 (1964) 236–242.
[2] Krokosky E.M., Krouskop T.A., A stress deformation model of the human aorta, J. Biomed. Mat. Res. 2 (1968) 503–525.
[3] Krokosky E.M., Krouskop T.A., The determination of the constitutive relationships for a human aorta, J. Biomed. Mat. Res. 4 (1970) 525–547.
[4] Timoshenko S.P., Goodier J.N., in: Theory of Elasticity, McGraw-Hill, New York, 1970, pp. 403–409.
[5] Saada S., Elasticity, Theory and Applications, Pergamon Press, New York, 1983.
[6] Fung Y.C., Biomechanical Properties of Living Tissues, Springer-Verlag, New York, 1981, Chapter 7.
[7] Anderson W.A.D., Pathology, C.V. Mosby, St. Louis, 1953.
[8] Garra B.S., Céspedes E.I., Ophir J., Spratt R.S., Zuurbier R.A., Magnant C.M., Pennanen M.F., Elastography of breast lesions: Initial clinical results, Radiology 202 (1997) 79–86.
[9] Kallel F., Ophir J., Magee K., Krouskop T., Elastographic imaging of low-contrast elastic modulus distributions in tissue, Ultrasound Med. Biol. 24 (1998) 409–425.
[10] Bakke T., A new mechanical instrument for the measurement of fibro-elasticity with special reference to its use in the assessment of the consistency of the uterine cervix, Acta Obstet. Gynecol. Scand. 52 (1973) 277–287.
[11] Chen E.J., Novakofski J., Jenkins W.K., O'Brien W.D. Jr., Young's modulus measurements of soft tissues with application to elasticity imaging, IEEE Trans. Ultras. Ferroel. Freq. Cont. 43 (1996) 191–194.
[12] D'Angelo E., Stress-strain relationships during uniform and non-uniform expansion of isolated lungs, Respir. Physiol. 23 (1975) 87–107.
[13] Fukaya H., Hildebrandt J., Martin C.J., Stress-strain relations of tissue sheets undergoing uniform two dimensional stretch, J. Appl. Physiol. 27 (1969) 758–762.
[14] Galey F.R., Elastic properties of fixed and fresh muscle, J. Ultrastruct. Res. 26 (1969) 424–441.
[15] Gao L., Parker K.J., Lerner R.M., Levinson S.F., Imaging of the elastic properties of tissue — A review, Ultrasound Med. Biol. 22 (1996) 959–977.
[16] Harley R., James D., Miller A., White J.W., Phonons and the elastic moduli of collagen and muscle, Nature 265 (1977) 285–287.
[17] Malinauskas M., Krouskop T.A., Barry P.A., Noninvasive measurement of the elastic modulus of tissue in the above-knee amputation stump, J. Rehab. Res. Dev. 26 (1989) 45–52.
[18] Sarvazyan A.P., Shear acoustic properties of soft biological tissues in medical diagnostics, J. Acoust. Soc. Am. Proc. 93 (1993) 2329.
[19] Yamada H., Strength of Biological materials, Williams & Wilkins, Baltimore, MD, 1970.
[20] Demiray H., A note on the elasticity of soft biological tissues, J. Biomech. 5 (1972) 309–311.
[21] Krouskop T.A., Vinson S., Goode B., Dougherty D., A pulsed Doppler ultrasonic system for making noninvasive measurements of the mechanical properties of soft tissue, J. Rehab. Res. Dev. 24 (1987) 1–8.
[22] Ophir J., Céspedes E.I., Ponnekanti H., Yazdi Y., Li X., Elastography: a quantitative method for imaging the elasticity of biological tissues, Ultrasonic Imag. 13 (1991) 111–134.
[23] Ophir J., Céspedes I., Garra B., Ponnekanti H., Huang Y., Maklad N., Elastography: ultrasonic imaging of tissue strain and elastic modulus in vivo, Eur. J. Ultrasound 3 (1996) 49–70.
[24] Ophir J., Kallel F., Varghese T., Bertrand M., Céspedes I., Ponnekanti H., Elastography: A systems approach, Int. J. Imag. Syst. Technol. (1997) 89–103.
[25] Cespedes I., Ophir J., Ponnekanti H., Maklad N., Elastography: elasticity imaging using ultrasound with application to muscle and breast in vivo, Ultrasonic Imag. 15 (1993) 73–88.
[26] Krouskop T.A., Wheeler T.M., Kallel F., Garra B., Hall T., The elastic moduli of breast and prostate tissues under compression, Ultrasonic Imag. 20 (1998) 151–159.
[27] O'Donnell M., Skovoroda A.R., Shapo B.M., Emelianov S.Y., Internal displacement and strain imaging using ultrasonic speckle tracking, IEEE Trans. Ultrason. Ferroel. Freq. Cont. 41 (1994) 314–325.
[28] Lerner R.M., Parker K.J., Sono-elasticity in ultrasonic tissue characterization and echographic imaging, in: Thijssen J.M. (Ed.), Proc. 7th Eur. Comm. Workshop, Nijmegen, The Netherlands, 1987.
[29] Lerner R.M., Huang S.R., Parker K.J., "Sonoelasticity" images derived from ultrasound signals in mechanically vibrated tissues, Ultrasound Med. Biol. 16 (1990) 231–239.
[30] Yamakoshi Y., Sato J., Sato T., Ultrasonic imaging of internal vibration of soft tissue under forced vibration, IEEE Trans. Ultrason. Ferroel. Freq. Cont. 37 (1990) 45–53.
[31] Alam S.K., Richards D.W., Parker K.J., Detection of intraocular pressure change in the eye using sonoelastic Doppler ultrasound, Ultrasound Med. Biol. 20 (1994) 751–758.

[32] Varghese T., Ophir J., A theoretical framework for performance characterization of elastography: The strain filter, IEEE Trans. Ultrason. Ferroel. Freq. Cont. 44 (1997) 164–172.
[33] Konofagou E.E., Ophir J., Kallel F, Varghese T., Elastographic dynamic range expansion using variable applied strains, Ultrasonic Imag. 19 (1997) 145–166.
[34] Varghese T., Bilgen M., Ophir J., Multiresolution imaging in elastography, IEEE Trans. Ultrason. Ferroel. Freq. Cont. 45 (1998) 65–75.
[35] Ponnekanti H., Ophir J., Huang Y., Céspedes I., Fundamental mechanical limitations on the visualization of elasticity contrast in elastography, Ultrasound Med. Biol. 21 (1995) 533–543.
[36] Kallel F., Bertrand M., Ophir J., Fundamental limitations on the contrast-transfer efficiency in elastography: An analytic study, Ultrasound Med. Biol. 22 (1996) 463–470.
[37] Varghese T., Ophir J., An analysis of elastographic contrast-to-noise ratio performance, Ultrasound Med. Biol. 24 (6) (1998) 915–924.
[38] Sarvazyan A.P., Skovoroda A.R., Emelianov S.Y., Flowkes J.B., Pipe J.G., Adler R.S., Buxton R.B., Carson P.L., Biophysical bases of elasticity imaging, Acoust. Imag. 21 (1995) 223–240.
[39] Ophir J., Alam S.K., Garra B.S., Kallel F., Konofgou E.E., Krouskop T.A., Varghese T., Elastography: measurement and imaging of tissue elasticity, Proc. Inst. Mech. Eng. 219 H (1999) 203–233.
[40] Alam S.K., Ophir J., Reduction of signal decorrelation from mechanical compression of tissues by temporal stretching: applications to elastography, Ultrasound Med. Biol. 23 (1997) 95–105.
[41] Céspedes I., Ophir J., Reduction of image noise in elastography, Ultrasonic Imag. 15 (2) (1993) 89–102.
[42] Alam S.K., Ophir J., Konofagou E.E., An adaptive strain estimator for Elastography, IEEE Trans. Ultrason. Ferroelec. Freq. Cont. 45 (1998) 461–472.
[43] Konofagou E.E., Ophir J., A new elastographic method for estimation and imaging of lateral displacements, lateral strains, corrected axial strains and Poisson's ratios in tissues, Ultrasound Med. Biol. 24 (1998) 1183–1199.
[44] Alam S.K., Ophir J., Céspedes I., Varghese T., A deconvolution filter for improvement of time-delay estimation in elastography, IEEE Trans. Ultrason. Ferroel. Freq. Cont. 45 (6) (1998) 1565–1572.
[45] Varghese T., Ophir J., The nonstationary strain filter in elastography, Part I – Frequency dependent attenuation, Ultrasound Med. Biol. 23 (1997) 1343–1356.
[46] Kallel F., Varghese T., Ophir J., Bilgen M., The nonstationary strain filter in elastography, Part II – Lateral and elevational decorrelation, Ultrasound Med. Biol. 23 (1997) 1357–1369.
[47] Alam S.K., Ophir J., Varghese T., Elastographic axial resolution criteria: An experimental study, IEEE Trans. Ultrason. Ferroel. Freq. Cont. 47 (1) (2000) 304–309.
[48] Kallel F., Prihoda C.D., Ophir J., Contrast transfer efficiency for continuously varying tissue moduli: simulation and phantom validation, Ultrasound Med. Biol. 27 (8) (2001) 1115–1125.
[49] Kallel F., Price R.E., Konofagou E.E., Ophir J., Elastographic Imaging of the normal canine prostate in vitro, Ultrasonic Imag. 21 (1999) 201–215.
[50] Righetti R., Kallel F., Stafford R.J., Price R.E., Krouskop T.A., Hazle J.D., Ophir J., Elastographic characterization of HIFU-induced lesions in canine livers, Ultrasound Med. Biol. 25 (7) (1999) 1099–1113.
[51] Kallel F., Ophir J., A least-squares estimator for elastography, Ultrasonic Imag. 19 (1997) 195–208.
[52] Konofagou E.E., Varghese T., Ophir J., Alam S.K., Power spectral strain estimators in elastography, Ultrasound Med. Biol. 25 (7) (1999) 1115–1129.
[53] Varghese T., Konofagou E.E., Ophir J., Alam S.K., Bilgen M., Direct strain estimation in elastography using spectral cross-correlation, Ultrasound Med. Biol. 26 (9) (2000) 1525–1537.
[54] Alam S.K., Lizzi F.L., Feleppa E.J., Varghese T., Novel estimators for elastography, in: Shung K.K., Insana M.F. (Eds.), Medical Imaging 2001, Ultrasonic Imaging and Signal Processing, Proceedings of SPIE, Vol. 4325, 2001, pp. 314–325.